

# Efficient Organic Solar Cells Enabled by Simple Non-Fused Electron Donors with Low Synthetic Complexity

Yueyue Gao, Minghuan Cui, Shengchun Qu, Huaping Zhao, Zhitao Shen, Furui Tan,\*  
Yulian Dong, Chaochao Qin,\* Zhijie Wang,\* Weifeng Zhang, Zhangguo Wang,  
and Yong Lei\*

Fused-ring electron donors boost the efficiency of organic solar cells (OSCs), but they suffer from high cost and low yield for their large synthetic complexity (SC > 30%). Herein, the authors develop a series of simple non-fused-ring electron donors, PF1 and PF2, which alternately consist of furan-3-carboxylate and 2,2'-bithiophene. Note that PF1 and PF2 present very small SC of 9.7% for their inexpensive raw materials, facile synthesis, and high synthetic yield. Compared to their all-thiophene-backbone counterpart PT-E, two new polymers feature larger conjugated plane, resulting in higher hole mobility for them, especially a value up to  $\approx 10^{-4}$  cm<sup>2</sup> V<sup>-1</sup> s for PF2 with longer alkyl side chain. Meanwhile, PF1 and PF2 exhibit larger dielectric constant and deeper electronic energy level versus PT-E. Benefiting from the better physicochemical properties, the efficiencies of PF1- and PF2-based devices are improved by  $\approx 16.7\%$  and  $\approx 71.3\%$  relative to that PT-E-based devices, respectively. Furthermore, the optimized PF2-based devices with introducing PC<sub>71</sub>BM as the third component deliver a higher efficiency of 12.40%. The work not only indicates that furan-3-carboxylate is a simple yet efficient building block for constructing non-fused-ring polymers but also provides a promising electron donor PF2 for the low-cost production of OSCs.

and short energy payback time et al.<sup>[1-4]</sup> Nowadays, the state-of-the-art photovoltaic performance of OSCs based on fused-ring polymers can indeed rival those of polycrystalline silicon solar cells.<sup>[5-10]</sup> However, fused-ring polymers always present large synthetic complexity (SC > 30%) due to their tedious synthetic procedures and complicated post-purification, which inevitably results in high cost (>1000 \$ g<sup>-1</sup>) and leads to that they can seldom be prepared in a high quantity (>10 g). The high cost, as well as poor scalability, greatly hamper the applications of fused-ring polymers in OSCs commercialization.<sup>[11-14]</sup> Therefore, developing polymers with low SC but still featuring good photovoltaic performance is urgent and significant for the further development of OSCs.

Compared to fused-ring polymers, poly(3-hexylthiophene) (P3HT) should be the admittedly simplest polymer applying in OSCs, which is not only ascribed to its simple molecular structure but also attributed to its facile synthesis.<sup>[15-17]</sup> Yet, most P3HT-based OSCs show inferior efficiency with value of less than 10%, which is partially ascribed to the shallow highest occupied molecular orbital energy ( $E_{\text{HOMO}}$ ) level of P3HT.<sup>[18-20]</sup> During the past decades, introducing electron-withdrawing groups or conjugated


## 1. Introduction

Organic solar cells (OSCs) have been paid extensive attention in academia and industry due to their unique characteristics, that is, light-weight, mechanical flexibility, environmental friendliness,

uted to its facile synthesis.<sup>[15-17]</sup> Yet, most P3HT-based OSCs show inferior efficiency with value of less than 10%, which is partially ascribed to the shallow highest occupied molecular orbital energy ( $E_{\text{HOMO}}$ ) level of P3HT.<sup>[18-20]</sup> During the past decades, introducing electron-withdrawing groups or conjugated

Y. Gao, Z. Shen, F. Tan, W. Zhang  
Key Laboratory of Photovoltaic Materials  
Henan University  
Kaifeng 475004, P. R. China  
E-mail: frtan@henu.edu.cn

M. Cui, C. Qin  
Henan Key Laboratory of Infrared Materials & Spectrum  
Measures and Applications  
Henan Normal University  
Xinxiang 453007, P. R. China  
E-mail: qinchaochao@htu.edu.cn

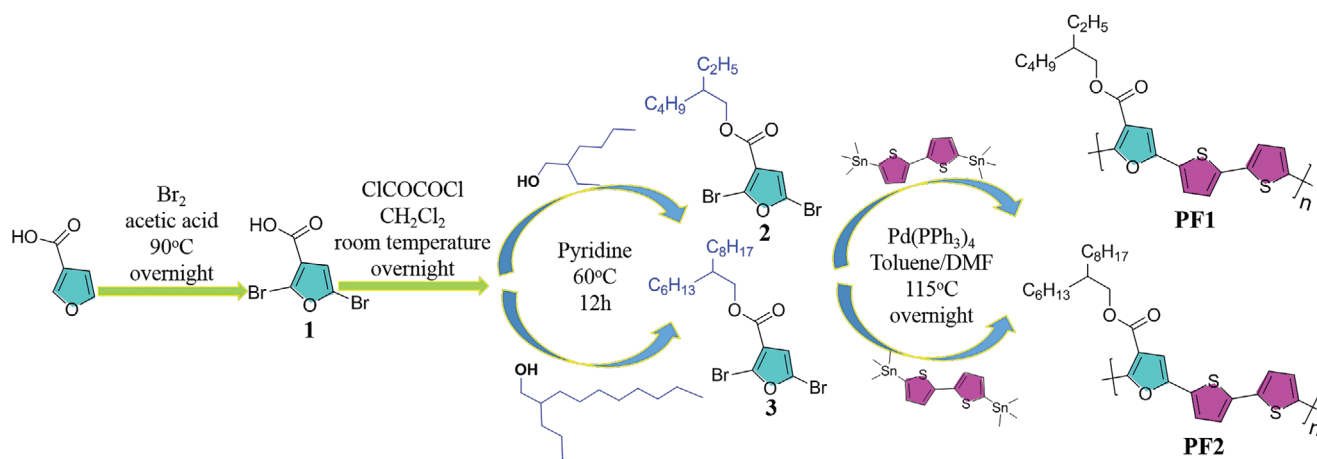
 The ORCID identification number(s) for the author(s) of this article can be found under <https://doi.org/10.1002/smll.202104623>.

© 2021 The Authors. Small published by Wiley-VCH GmbH. This is an open access article under the terms of the Creative Commons Attribution License, which permits use, distribution and reproduction in any medium, provided the original work is properly cited.

S. Qu, Z. Wang, Z. Wang  
Key Laboratory of Semiconductor Materials Science  
Beijing Key Laboratory of Low Dimensional Semiconductor Materials  
and Devices  
Institute of Semiconductors  
Chinese Academy of Sciences  
Beijing 100083, P. R. China  
E-mail: wangzj@semi.ac.cn

H. Zhao, Y. Dong, Y. Lei  
Fachgebiet Angewandte Nanophysik  
Institut für Physik & IMN MacroNano  
Technische Universität Ilmenau  
98693 Ilmenau, Germany  
E-mail: yong.lei@tu-ilmenau.de

DOI: 10.1002/smll.202104623



**Scheme 1.** The synthetic route of PF1 and PF2.

side chains to polythiophene (PT) has been found to be effective in deepening the  $E_{\text{HOMO}}$  level versus that of P3HT, which enables a gradual increase of the PCE surpassing 12%.<sup>[21–24]</sup> However, the hole mobility of those efficient PT derivatives is inversely lower than P3HT for their dissatisfactory molecular coplanarity.<sup>[25]</sup> Moreover, owing to the additional synthetic procedures, the SC of those efficient PT derivatives is still large with value exceeding 20%, which still results in high cost for those efficient PT derivatives.<sup>[22]</sup> Hence, seeking other effective strategies, such as simply doing modification on the molecular backbone of PT, should be important and anticipated for constructing simple polymers simultaneously featuring low SC, high hole mobility, and effective photovoltaic performance.

As the analogs of thiophene, furan and its derivatives feature smaller volume, larger dipole moment, and lower dewar resonance energy.<sup>[26–28]</sup> Meanwhile, the higher electronegativity of oxygen in furan than sulfur in thiophene could impart furan-based photovoltaic materials more stabilized  $E_{\text{HOMO}}$  level.<sup>[29,30]</sup> Moreover, furan and its derivatives are indisputably sustainable owing to that they can be derived from biomass, whereas starting materials derived from fossil fuels are not. Therefore, furan and its derivatives should possess great potential for low-cost synthesis of photovoltaic materials.<sup>[31–33]</sup>

Taking into the advantages of furan, herein, we designed and synthesized two simple non-fused-ring electron donors PF1 and PF2 via copolymerizing furan-3-carboxylate with 2,2'-bithiophene. Note that the SC of two new polymers is as small as 9.7%. And PF1 and PF2 feature larger conjugated plane and higher hole mobility than their all-thiophene-backbone counterpart PT-E. Especially, the hole mobility of PF2 with longer alkyl side chain could approach up to  $\approx 10^{-4} \text{ cm}^2 \text{ V}^{-1} \cdot \text{s}$ . Beyond that, PF1 and PF2 demonstrate larger dielectric constant and deeper  $E_{\text{HOMO}}$  level than PT-E. When fabricated OSCs with polymer (PT-E, PF1, or PF2) as electron donor and m-ITIC as electron acceptor, PT-E:m-ITIC based devices produce a decent PCE of 6.41%. However, benefiting from the better physicochemical properties, the PCEs of PF1- and PF2-based devices are increased by  $\approx 16.7\%$  and  $\approx 71.3\%$  relative to PT-E-based devices, respectively. Moreover, the optimized PF2-based devices with introducing PC<sub>71</sub>BM as the third component deliver a higher efficiency of 12.40%.

## 2. Results and Discussion

### 2.1. Materials Synthesis and Properties

The synthetic route of PF1 and PF2 is outlined in **Scheme 1**, and the detailed synthetic procedures are described in Supporting Information. As is shown, PF1 and PF2 can be easily synthesized via only three steps as well as cost-effective raw materials. For comparison, their analog polymer PT-E with all-thiophene-unit backbone was also prepared according to the work reported by Zhang et al. (Supporting Information).<sup>[34]</sup> The molecular structures of the intermediates, PF1 and PF2 were confirmed by <sup>1</sup>H-NMR, <sup>13</sup>C-NMR, FTIR, and element analysis (Figures S1–S10, Supporting Information). PF1, PF2, and PT-E present amorphous characteristic but show good thermal stability with decomposing temperature (5% weight loss) exceeding 300 °C and stronger endurance against air and continuous heating (Figure S11, Supporting Information). It is noted that PF1 and PF1:m-ITIC film present stronger light endurance than that of PT-E and PT-E:m-ITIC film, respectively (Figure S12, Supporting Information), considering the same alkyl side chains and comparable molecular weight of PT-E and PF1. Three polymers display good solubility in halogenated solvents, that is, chloroform, chlorobenzene, and dichlorobenzene. The number average molecular weights ( $M_n$ ) of PT-E, PF1, and PF2 are 7.9, 10.5, and 30.1 kg mol<sup>-1</sup>, respectively, where the larger  $M_n$  of PF1 and PF2 should be ascribed to the better solubility of furan-based acceptor unit, being conducive to obtaining a better photon harvesting capability and a more favorable film morphology.<sup>[35–37]</sup>

### 2.2. Theoretical Calculation

To firstly give an understanding of structural difference among PT-E, PF1, and PF2, density functional theory (DFT) calculation at B3LYP/6-31G\* level on the dimer of three polymers was performed. As displayed in **Figure 1b**, the dihedral angles between thiophene-3-carboxylate and neighboring thiophene

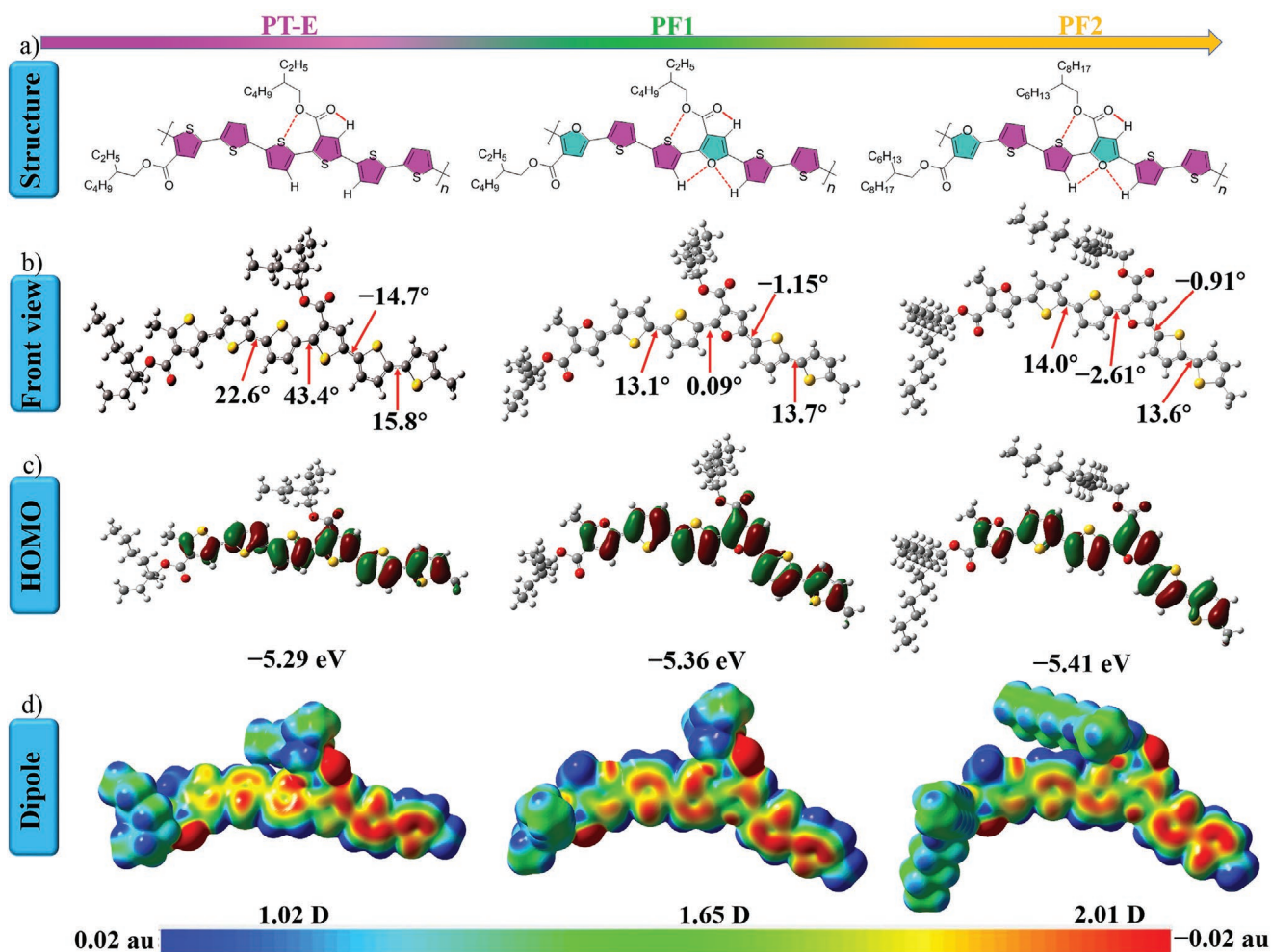


**Figure 1.** Theoretical calculation of PT-E, PF1, and PF2. a) Structures; b) Front view of optimized geometry; c) Simulated HOMO orbitals and  $E_{HOMO}$  levels; d) ESP and dipole moment.

in PT-E are  $43.4^\circ$  and  $-14.7^\circ$ , respectively. However, the corresponding values between furan-3-carboxylate and neighboring thiophene in PF1 and PF2 are reduced to  $0.09^\circ/-1.15^\circ$  and  $-2.61^\circ/-0.91^\circ$ , respectively. The almost planar backbone of PF1 and PF2 (Figure S13, Supporting Information) results from the synergistic effect of the small volume of furan and non-covalent interactions in PF1 and PF2 ( $C-O \cdots H$ ,  $O \cdots S$ , and  $C=O \cdots H$ ).<sup>[38–40]</sup> Compared to PT-E, the  $E_{HOMO}$  levels of PF1 and PF2 are deepened by 0.07 and 0.12 eV (Figure 1c), respectively, which should be ascribed to the stronger electronegativity of oxygen atom in furan relative to sulfur atom in thiophene.<sup>[39–41]</sup> As shown in Figure 1d, even though exhibiting similar continuous electrostatic potential (ESP), the dimer of PF1 and PF2 both display larger dipole moments than that of the dimer of PT-E, indicating that PF1 and PF2 might also feature larger dipole moment versus that of PT-E, which is confirmed by their larger relative dielectric constant than PT-E (Figure S14, Supporting Information). Therefore, efficient exciton dissociation and charge transportation could be expected for OSCs based on PF1 or PF2.<sup>[42–44]</sup>

### 2.3. Optical and Electrochemical Properties

PF1 and PF2 in diluted chlorobenzene solution display red-shifted absorption peaks ( $\lambda_{max}$ ) at 531 and 538 nm accompanied with enlarged absorption coefficient versus that of PT-E (Figure 2a and Table S1, Supporting Information). The optical bandgap ( $E_{gap}^{opt}$ ) of PT-E, PF1 and PF2 can be deduced from their absorption spectra onset in the film state (Figure 2b), corresponding to 1.88, 1.83, and 1.82 eV, respectively. It is noticed that three polymers demonstrate complementary absorption with the non-fullerene acceptor m-ITIC, which could maximize the photon flux and benefit for improving the photocurrent of derived OSCs.

The characterization via cyclic voltammetry could approximately estimate the  $E_{HOMO}/$ lowest unoccupied molecular orbital energy ( $E_{LUMO}$ ) levels of PT-E and PF1 locating at  $-5.21/-3.09$  eV and  $-5.33/-3.10$  eV, respectively (Figure 2c and Figure S15, Supporting Information), consistent with the trends determined via DFT calculations. Notably, extending the side-chain further deepens the  $E_{HOMO}/E_{LUMO}$  levels to

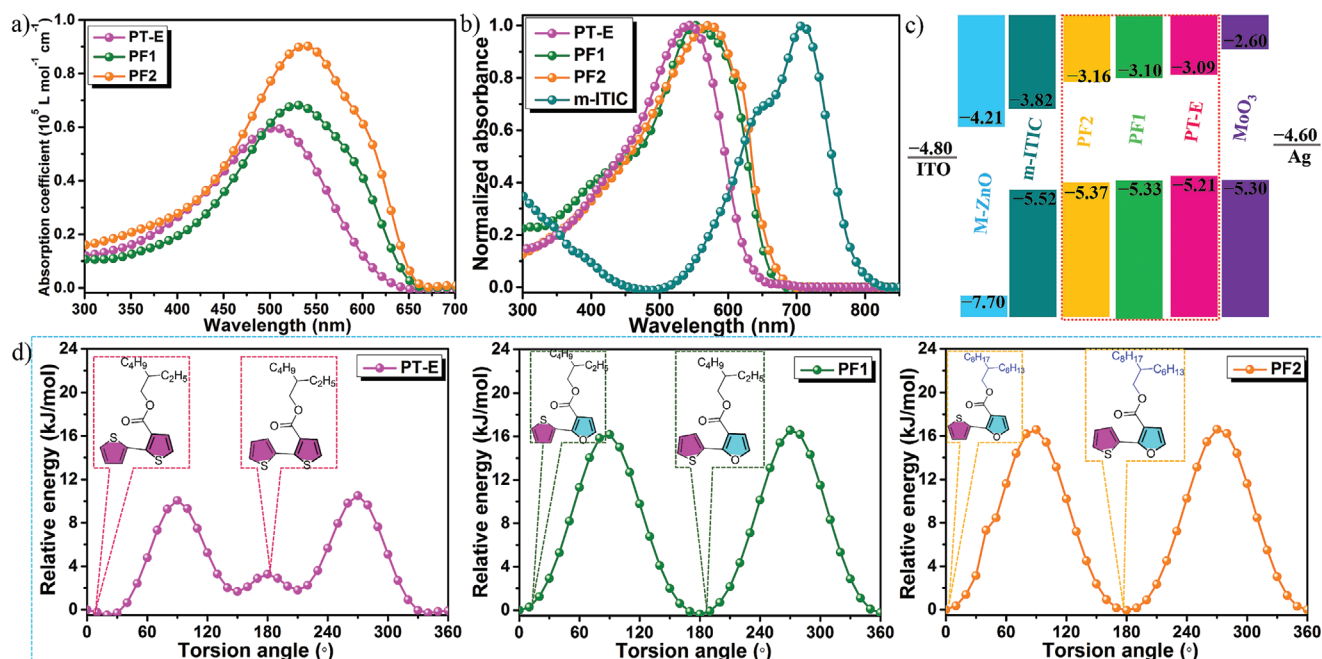


**Figure 2.** a) UV-Vis absorption spectra of PT-E, PF1, and PF2 in solution; b) Normalized UV-Vis absorption spectra of PT-E, PF1, PF2, and m-ITIC in film; c) Energy level diagram of materials utilized in OSCs of this work; d) The energy-torsion angle curves of PT-E, PF1, and PF2 from DFT calculation.

−5.37/−3.16 eV for PF2. The small  $E_{\text{HOMO}}$  offsets at PF1:m-ITIC (0.19 eV) or PF2:m-ITIC (0.15 eV) benefit for low charge transfer energy loss while remaining high charge transfer efficiency, being confirmed by the high fluorescence quenching efficiency (93.4% and 96.7%) of m-ITIC when blended with PF1 or PF2 (Figure S16, Supporting Information).<sup>[45]</sup>

As depicted in Figure 2d, PT-E not only shows three metastable states but also depicts a small energy barrier of 9.97 kJ mol<sup>−1</sup> for the rotation from stable state (0°) to metastable state (90°), while the corresponding values increase to 16.24 and 16.69 kJ mol<sup>−1</sup> for PF1 and PF2, respectively, which indicates that PF1 and PF2 feature better planarity than PT-E. The above result is further confirmed by the higher hole mobility for PF1 (0.28 × 10<sup>−4</sup> cm<sup>2</sup> V<sup>−1</sup> · s) and PF2 (0.91 × 10<sup>−4</sup> cm<sup>2</sup> V<sup>−1</sup> · s) than PT-E (0.17 × 10<sup>−4</sup> cm<sup>2</sup> V<sup>−1</sup> · s), which is measured from space-charge-limited current model (Figure S9, Supporting Information). It is noted that the hole mobility of PF2 is highly approachable to that of P3HT relative to those efficient PT derivatives.<sup>[46–48]</sup>

## 2.4. Photovoltaic Properties

The photovoltaic properties of PT-E, PF1, and PF2 were evaluated in OSCs with an invert architecture of ITO/M-ZnO/active layer/MoO<sub>3</sub>/Ag (Figure 3a), where M-ZnO is prepared by modifying ZnO film via a trisiloxane molecule (Figure S18, Supporting Information), and m-ITIC was adopted as the electron acceptor. To carefully optimize the photovoltaic performance of devices, a series of parameters were finely tuned, that is, concentration of electron donors, weight ratio of electron donor:m-ITIC, additive, thermal annealing et al. (Figures S19–S30, Supporting Information). As shown in Figure 3b, the optimized PT-E:m-ITIC devices show a decent PCE of 6.41%. Moreover,

for further improving the efficiency of PT-E based devices, PT-E with larger molecular weight was also prepared. However, similar devices based on PT-E:m-ITIC but adopting PT-E with higher molecular weight produce a poor PCE of 5.10%, which should be ascribed to the much worse morphology of derived blend film (Figure S31, Supporting Information). Compared to PT-E based devices, the PCE of PF1:m-ITIC and PF2:m-ITIC based devices could be improved to 7.48% and 10.98%, respectively. It is noted that all photovoltaic parameters of PF1- and PF2-based devices are enhanced relative to PT-E-based devices, where the enhancement of  $V_{\text{oc}}$  for the former should be attributed to their deeper  $E_{\text{HOMO}}$  levels, and the increased FF should be assigned to the higher and more balanced charge mobilities of PF1- and PF2-based devices (Table 1). For the improvement of  $J_{\text{sc}}$  for PF1- and PF2-based devices, it not only originates from their enlarged absorption coefficient versus PT-E, but also correlates well with the proficient charge dynamics of their derived devices (discuss in later).

Interestingly, when replacing 6% m-ITIC with same amount of PC<sub>71</sub>BM, the derived devices could produce an enhanced PCE of 11.45% with an increased  $J_{\text{sc}}$  of 1783 mA cm<sup>−2</sup> and an intensified FF of 74.1% but a slightly reduced  $V_{\text{oc}}$  of 0.867 V (Figure S32, Supporting Information). Compared to binary devices, the decreased  $V_{\text{oc}}$  of ternary devices should be ascribed to the relatively deeper  $E_{\text{LUMO}}$  level of PC<sub>71</sub>BM versus that of m-ITIC.<sup>[49,50]</sup> Further replacing 12% m-ITIC with same amount of PC<sub>71</sub>BM could impart a higher PCE of 12.40% with a remarkable FF of 77.6% for derived devices, which is resulted from the better morphology of the derived blend film featuring finely nano-scale interpenetrating networks as well as uniform and smooth surface with small root mean square (RMS) roughness of 1.16 nm (Figure S33a–c, Supporting Information). Exceeding 12% PC<sub>71</sub>BM in the ternary blend film, the efficiency of



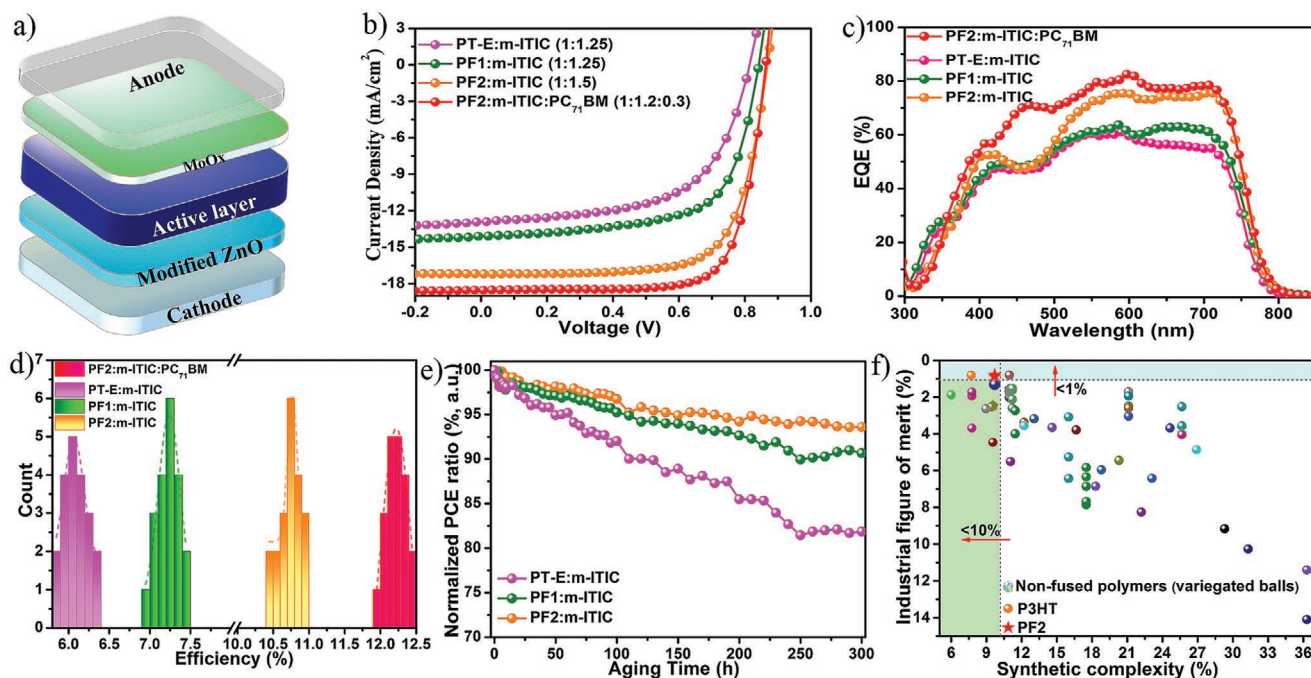


**Figure 3.** a) Schematic illustration of device architecture in this work; b)  $J$ - $V$  characteristics and c) EQE spectra of those optimized devices; d) Distribution of PCE for those optimized devices; e) Normalized PCE for those optimized devices with continuous illumination ( $100 \text{ mW cm}^{-2}$ ) in  $\text{N}_2$  for different time; f) Plots of industrial figure of merit and SC of P3HT, PF2, and reported non-fused-ring simple polymers.

derived devices would be highly impaired for their simultaneously reduced photovoltaic parameters. Especially, completely replacing m-ITIC with  $\text{PC}_{71}\text{BM}$  would result in a poor PCE of 6.35%, which correlates with the limited absorption ability as well as the poor morphology with relatively severe phase separation and rough surface with large RMS roughness of 3.18 nm for the derived blend film (Figure S33b–f, Supporting Information). On the other hand, replacing m-ITIC with the famous acceptor Y6, the devices based on PF2:Y6 conversely produce a poor photovoltaic performance (Figure S34, Supporting Information), which should be ascribed to the completely homogeneous bulk morphology without obvious phase separation resulting from the better miscibility between PF2 and Y6 (Figure S35, Supporting Information), and the similar phenomenon was also reported by Geng et al.<sup>[21]</sup>

As shown in Figure 3c, the  $J_{\text{sc}}$  values integrated from the external quantum efficiency (EQE) spectra agree with the  $J_{\text{sc}}$  values obtained from the  $J$ - $V$  measurement. Additionally, the reproducibility of photovoltaic performance of those optimized

devices is examined. As depicted in Figure 3d, the average PCEs with deviation are  $6.08 \pm 0.14\%$ ,  $7.21 \pm 0.14\%$ ,  $10.74 \pm 0.15\%$ , and  $12.22 \pm 0.12\%$  for each repetitive 20 devices based on PT-E:m-ITIC, PF1:m-ITIC, PF2:m-ITIC, and PF2:m-ITIC:PC<sub>71</sub>BM, respectively. Moreover, PF1:m-ITIC and PF2:m-ITIC based devices exhibit better operational stability than PT-E:m-ITIC or P3HT:m-ITIC based devices (Figure 3e and Figure S36, Supporting Information). Among them, the superior photovoltaic performance of PF2-based devices not only originates from the better optoelectronic property of PF2, but also be from the highly improved charge dynamics behavior, that is, faster charge transport, more efficient charge collection, and fewer charge recombination. Besides, the morphology of PF2:m-ITIC layer also presents an additional positive effect on the improved photovoltaic performance of PF2-based devices.

Furthermore, we investigate the cost-effectiveness of three polymers concerning the SC and material cost (MC) according to the reported work (Tables S2–S11, Supporting Information).<sup>[11,51]</sup> It is pointed that PT-E shows a SC of 9.55% coupled with an MC

**Table 1.** Photovoltaic performance of those optimized devices.

Active layer	$V_{\text{oc}}$ [V]	$J_{\text{sc}}$ [ $\text{mA cm}^{-2}$ ]	FF [%]	PCE [%]	$\mu_{\text{h}}^{\text{e)}$	$\mu_{\text{e}}^{\text{e)}$	$\mu_{\text{e}}/\mu_{\text{h}}$
PT-E:m-ITIC <sup>a)</sup>	0.82 ( $0.82 \pm 0.01$ )	13.07 ( $12.62 \pm 0.36$ )	59.8 ( $58.9 \pm 1.7$ )	6.41 ( $6.08 \pm 0.14$ )	0.33	0.64	1.93
PF1:m-ITIC <sup>b)</sup>	0.84 ( $0.84 \pm 0.02$ )	14.11 ( $13.80 \pm 0.30$ )	63.1 ( $62.2 \pm 1.2$ )	7.48 ( $7.21 \pm 0.14$ )	1.22	1.51	1.24
PF2:m-ITIC <sup>c)</sup>	0.87 ( $0.87 \pm 0.14$ )	17.17 ( $16.96 \pm 0.17$ )	73.5 ( $72.8 \pm 0.8$ )	10.98 ( $10.74 \pm 0.15$ )	6.81	7.90	1.16
PF2:m-ITIC:PC <sub>71</sub> BM <sup>d)</sup>	0.86 ( $0.86 \pm 0.01$ )	18.52 ( $18.36 \pm 0.22$ )	77.6 ( $77.1 \pm 0.5$ )	12.40 ( $12.22 \pm 0.12$ )	9.44	10.3	1.09

The optimized thickness values of active layer are: <sup>a)</sup>96 nm; <sup>b)</sup>105 nm; <sup>c)</sup>118 nm, and; <sup>d)</sup>109 nm respectively; <sup>e)</sup>The units of  $\mu_{\text{h}}$  and  $\mu_{\text{e}}$  are  $10^{-4} \text{ cm}^2 \text{ V}^{-1} \text{ s}$ .

of  $\approx 29.1 \text{ \$ g}^{-1}$ . Even though the SC of PF1 and PF2 is slightly increased to 9.7%, PF1, and PF2 but present a lower MC of  $\approx 23.1$  and  $\approx 19.0 \text{ \$ g}^{-1}$ , respectively, which is ascribed to the higher synthetic yield of PF1 and PF2 than PT-E. Importantly, the MC of PF2 is very small than those reported efficient fused-ring polymers (Figure S38, Supporting Information).<sup>[11]</sup> Moreover, PF2 simultaneously presents small SC and industrial figure of merit (IFOM =  $\frac{\text{SC}}{\text{PCE}}$ ) among those reported non-fused-ring simple polymers (Figure 3f, Figure S37, Schemes S6–S31, and Tables S2–S11, Supporting Information). Considering the small SC and IFOM, low MC, and good photovoltaic efficiency, PF2 demonstrates great potential for low-cost production of efficient OSCs.<sup>[22]</sup> Moreover, these results also demonstrate that furan-3-carboxylate should be a simple and attractive building block for constructing low-cost and effective non-fused-ring polymers.

## 2.5. Charge Dynamics

Transient absorption (TA) spectra were conducted to investigate the charge dynamics in those optimized devices. As exhibited in Figure 4a–c, a bleaching signal at  $\approx 750 \text{ nm}$  can be observed for m-ITIC neat film, PF1:m-ITIC film, and PF2:m-ITIC film when excited by 730 nm mono-light. This signal, locating in the absorption region of m-ITIC, should be attributed to the ground state bleaching of the transition in m-ITIC. Besides, as the excitation photon energy (730 nm) is smaller than that is required for exciting PF1 and PF2, the two additional bleaching signals detected at  $\approx 550$  and  $\approx 600 \text{ nm}$  in the TA spectra of PF1:m-ITIC film and PF2:m-ITIC film are only assigned to the hole transfer from m-ITIC to PF1 or PF2

especially considering the shallower  $E_{\text{LUMO}}$  level of m-ITIC than that of PF1 or PF2.<sup>[52]</sup>

As shown in TA spectra with a normalized scale (Figure 4d), the relaxation rates of PF1:m-ITIC film ( $\approx 1.0 \text{ ps}$ ) and PF2:m-ITIC ( $\approx 1.0 \text{ ps}$ ) film are faster than that of m-ITIC neat film ( $\approx 3.0 \text{ ps}$ ). Moreover, the buildup of the signals probed at  $\approx 550 \text{ nm}$  in PF1:m-ITIC film and PF2:m-ITIC film is prolonged with the lifetime of onset exponential growth increasing to  $\approx 0.6$  and  $\approx 1.0 \text{ ps}$ , respectively (Figure 4e), further confirming the hole transfer is the main origin of the additional bleaching signals for PF1:m-ITIC film and PF2:m-ITIC film. The comparatively slow TA decay of PF2:m-ITIC film suggests its charge recombination rate is highly suppressed. Besides, the prolonged TA decays of PF1:m-ITIC film and PF2:m-ITIC film excited by 500 nm (Figure 4f and Figure S39, Supporting Information) indicate the electron transfer is efficient in both optimized films.

To further clarify the charge extraction process of those optimized devices, transient photocurrent (TPC) and light intensity ( $P_{\text{light}}$ )-dependent  $J_{\text{sc}}$  measurements were conducted. As shown in Figure 5a, PF2:m-ITIC based devices demonstrate a more efficient charge extraction evaluated from a smaller photocurrent decay lifetime of  $\approx 9.33 \text{ ns}$ , while the corresponding values increase to  $\approx 14.38$  and  $\approx 18.99 \text{ ns}$  for PF1:m-ITIC and PT-E:m-ITIC devices, respectively. Meanwhile, a larger  $\alpha$  (0.988) more close to unity for PF2:m-ITIC based devices also suggests a more balanced and faster charge extraction in this device (Figure 5b), agreeing with its enlarged and balanced charge mobilities (Table 1 and Figure S40, Supporting Information). The transient photoluminescence (TRPL) spectrum of PF2:m-ITIC film with a smaller lifetime of  $\approx 0.79 \text{ ns}$  confirms an efficient charge transfer (Figure 5c). The proficient charge extraction usually suppresses

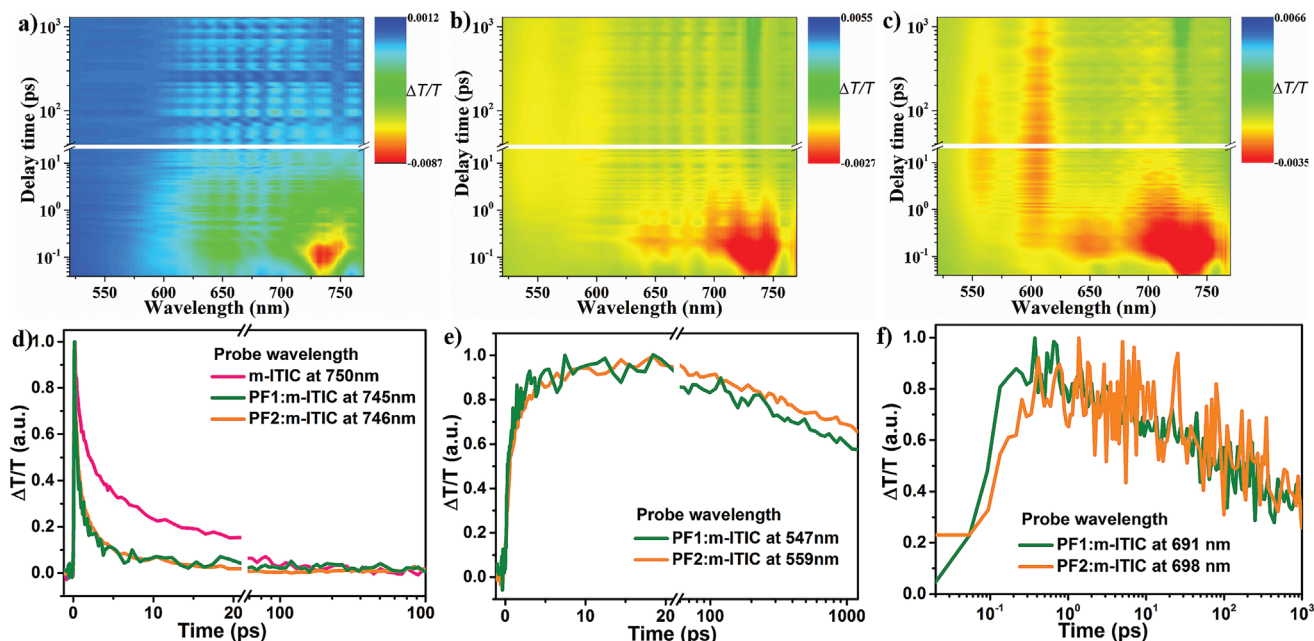


**Figure 4.** Transient absorption signals recorded from a) m-ITIC neat film, b) PF1:m-ITIC film, and c) PF2:m-ITIC film excited by 730 nm and probed at  $\approx 750 \text{ nm}$ . d) Dynamics probed at  $\approx 750 \text{ nm}$  recorded from m-ITIC neat film, PF1:m-ITIC film, and PF2:m-ITIC film excited by 730 nm. e) Dynamics probed at  $\approx 550 \text{ nm}$  recorded from PF1:m-ITIC film and PF2:m-ITIC film excited by 730 nm. f) Dynamics probed at  $\approx 700 \text{ nm}$  recorded from PF1:m-ITIC film and PF2:m-ITIC film excited by 500 nm.

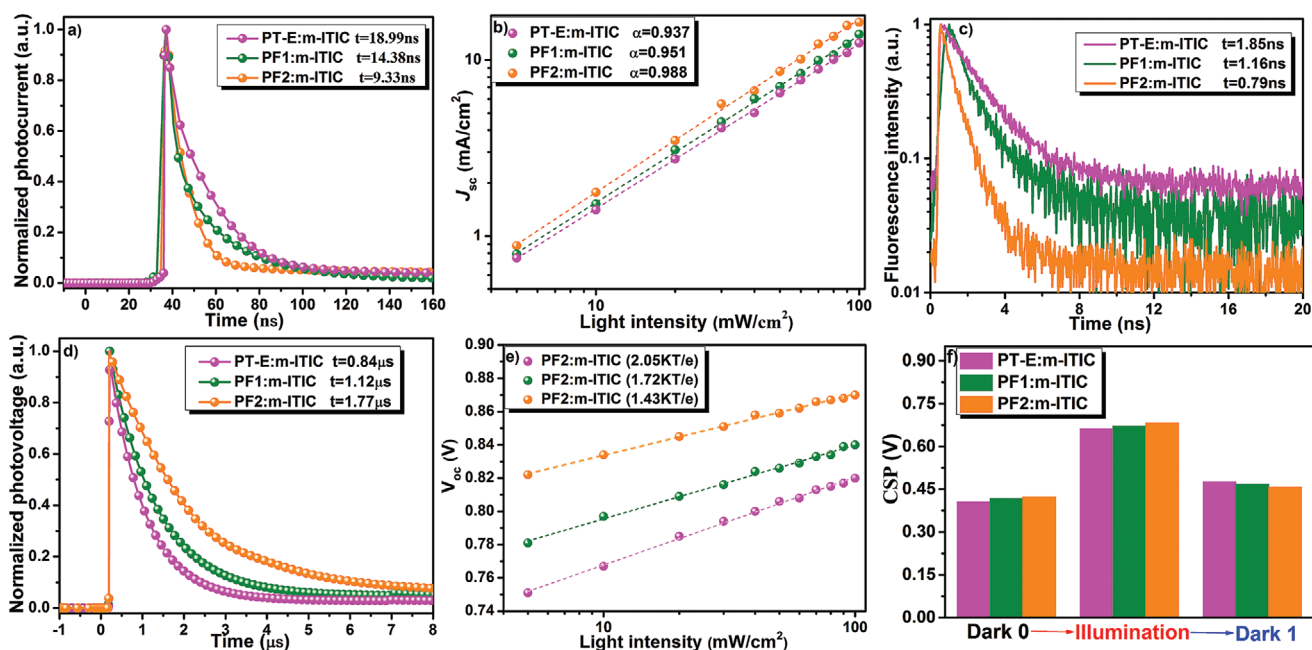


**Figure 5.** a) TPC spectra of those optimized devices; b)  $J_{sc}$  of those optimized devices as a function of  $P_{light}$ ; c) TRPL spectra of those optimized films; d) TPV spectra of those optimized devices; e)  $V_{oc}$  of those optimized devices as a function of  $P_{light}$ , and the relationship between  $P_{light}$  and  $V_{oc}$  follows the equation:  $V_{oc} \propto n(kT/q) \ln P_{light}$ , where  $k$ ,  $T$ , and  $q$  represent Boltzmann constant, temperature in Kelvin, and elementary charge, respectively. In general, the slope of  $n(kT/q)$  approaches  $kT/q$  when trap-assisted recombination is suppressed; f) CSP of the optimized films measured at Dark 0, under illumination, at Dark 1.

bimolecular recombination and contributes to the improvement of photovoltaic performance.<sup>[53–55]</sup>

To evaluate the charge recombination aforementioned, transient photovoltage (TPV) spectra were implemented. As depicted in Figure 5d, PF2:m-ITIC devices present a prolonged lifetime of  $\approx 1.77 \mu\text{s}$  compared to PT-E:m-ITIC devices ( $0.84 \mu\text{s}$ ) and PF1:m-ITIC devices ( $1.12 \mu\text{s}$ ), implying the charge recombination rate is significantly reduced in the former sample.<sup>[56]</sup> Furthermore, a smaller ideality factor  $n$  of 1.43 for PF2:m-ITIC devices also demonstrates the trap-assisted recombination is weaker in PF2:m-ITIC based devices than that in the other two devices (Figure 5e).

The contact surface potential (CSP) of those optimized films was alternately measured under dark and light illumination. The CSP values of each film firstly increased and then decreased following the light was turned on and off (Figure 5f). A discrepancy between the two dark CSP values was recorded and used to evaluate the density of charge traps that prevented the recovery of the CSP values from illumination to dark.<sup>[57]</sup> Compared to PT-E:m-ITIC and PF1:m-ITIC samples, PF2:m-ITIC sample generated a smaller CSP discrepancy of 0.034 V between dark 1 and dark 0 (Figure 5f, Figure S41, and Table S12, Supporting Information), suggesting fewer charges were captured by fewer traps, which was consistent with the result of TPV.

## 2.6. Morphology Properties

A series of morphological characterizations were performed and the results are shown in Figure 6. The optimized PT-E:m-ITIC film exhibits many grains distribution with large RMS roughness

of 756 nm (Figure 6a,b). The large bulk phase separation of PT-E:m-ITIC film should be assigned to poor miscibility between PT-E and m-ITIC, which is not only confirmed by the short interchain distance of PT-E ( $d_{lamellar}$ , 21.4 Å, Figure S28, Supporting Information) less than the molecular size of m-ITIC (22.0 Å, Figure S43, Supporting Information), but also evidenced by the large Flory–Huggins interaction parameter  $\chi$  of 1.49 between PT-E and m-ITIC (Figure S44, Supporting Information).<sup>[40]</sup> In comparison, PF1 and m-ITIC present enhanced miscibility with reduced  $\chi$  (1.03, Figure S44, Supporting Information), which results in nanoscale fibrillar textures-like interpenetrating network with a small RMS roughness (2.79 nm, Figure 6e,f). However, few large m-ITIC aggregation could be found in the optimized PF1:m-ITIC film (Figure 6f), which should be ascribed to the smaller  $d_{lamellar}$  of PF1 of 18.7 Å (Figure S45, Supporting Information). Comparatively, PF2 not only shows a further enhanced miscibility ( $\chi = 0.86$ ) with m-ITIC, but also presents a large  $d_{lamellar}$  of 22.2 Å allowing m-ITIC molecules facile interdigitation (Figure S46, Supporting Information). Therefore, PF2:m-ITIC film demonstrates a well-defined bicontinuous interpenetrating network with a uniform and smooth surface rich of nanofibrils (RMS = 1.88 nm, Figure 6i,j), which is highly conducive to charge transfer and transport as well as suppressing charge recombination.

We further applied depth-dependent X-ray photoelectron spectroscopy to clarify the vertical phase distribution in those optimized films, where the phase density ratio of Polymer – rich region ( $R_p$ ) was adopted as a tracking parameter (Figures S47–S49 and Tables S13–S15, Supporting Information).<sup>[58–60]</sup> It is found that PF2:m-ITIC optimized film



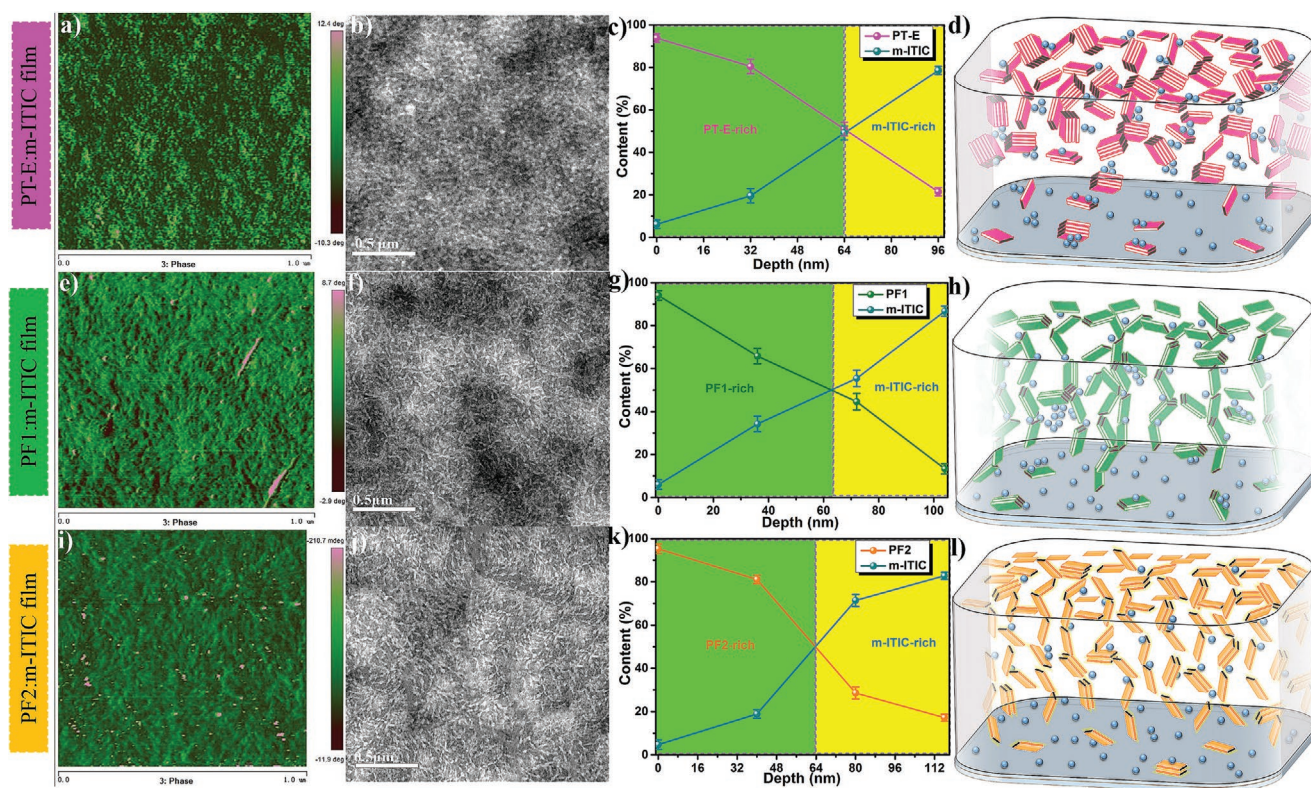


**Figure 6.** AFM phase images (a,e,i) and TEM images (b,f,j) of the optimized films; Calculated polymer or m-ITIC content in the optimized films (c,g,k) versus the film depth; The schematic diagram of the optimized films (d,h,l), where block and sphere represents PTs and m-ITIC, respectively.

shows a small  $R_p$  of 1.1 (Figure 6k), while the corresponding values increase to 1.9 and 1.5 for PT-E:m-ITIC and PF1:m-ITIC optimized films (Figure 6c,g), respectively. From the aforementioned results, we can depict the vertical phase distribution in three optimized films (Figure 6d,h,l). Comparatively, PF2:m-ITIC optimized film features a relatively ideal P-i-N vertical structure with PF2 and m-ITIC mainly located on the upper and bottom of their optimized film, respectively. This kind of vertical distribution is greatly beneficial for exciton dissociation, charge transportation, and collection, contributing to the superior photovoltaic performance for PF2:m-ITIC based devices.<sup>[61–63]</sup>

### 3. Conclusion

In summary, two simple non-fused-ring electron donors, PF1 and PF2, were designed and synthesized via copolymerizing furan-3-carboxylate and 2,2'-bithiophene. Owing to facile synthesis, inexpensive raw materials, and high yield, PF1 and PF2 present low SC of 9.7%. Meanwhile, PF1 and PF2 show larger conjugated plane, higher hole mobility, larger dielectric constant, and deeper electronic energy level than their all-thiophene-backbone counterpart PT-E. Benefiting from the better physicochemical properties, the efficiencies of PF1- and PF2-based devices are improved by  $\approx 16.7\%$  and  $\approx 71.3\%$ , respectively, in comparison with PT-E-based devices. Moreover, the optimized PF2-based devices with introducing suitable PC<sub>71</sub>BM as the third component deliver a higher efficiency of 12.40%. Our

work demonstrates that furan-3-carboxylate should be a promising building block for constructing low-cost and effective non-fused-ring polymers, and PF2 should feature high potential for low-cost large-scale production of efficient OSCs.

### 4. Experimental Section

**Materials:** Anhydrous toluene and dichloromethane were dried over sodium/benzophenone and calcium hydride, respectively. m-ITIC and PC<sub>71</sub>BM were purchased from Solarmer Materials Inc. Besides, furan-3-carboxylic acid, 5,5'-bis(trimethylstannyl)-2,2'-bithiophene and other chemicals applied in this work were purchased from Energy Chemical in China and were used as received without further purification. PT-E was synthesized according to the reported literature.<sup>[34]</sup> The detailed synthetic procedures and characterizations of the intermediates of PF1 and PF2 were provided in Supporting Information.

**Synthesis of PF1:** Monomer 2 (95.5 mg, 0.25 mmol), 5,5'-bis(trimethylstannyl)-2,2'-bithiophene (123.0 mg, 0.25 mmol) and toluene/DMF (10 mL/1 mL) were placed into a single-neck bottom-flask (25 mL). Then, the flask was vacuumed and refilled with N<sub>2</sub> three times. 0.01 mmol Pd(PPh<sub>3</sub>)<sub>4</sub> (11.5 mg) was quickly added into the flask, and the flask was vacuumed and refilled with N<sub>2</sub> once again. Next, the flask was placed into an oil-bath with the temperature at 110 °C, and kept stirring for 6.0 h under N<sub>2</sub> atmosphere. Subsequently, another batch of Pd(PPh<sub>3</sub>)<sub>4</sub> (5.8 mg, 0.005 mmol) was quickly added into the flask, and the mixture was further stirred at 110 °C for overnight. Afterward, 1.00 mmol phenyltri-*n*-butyltin (home-made) was injected into the flask and the mixture was consecutively stirred for 1.0 h. Then, 1.05 mmol 2-bromobenzene was also injected into the flask and the mixture was further consecutively stirred for 1.0 h. Next, the mixture was poured into 100 mL methanol and consecutively stirred for 2.0 h at room



temperature. After the precipitate was filtered, the solid was dissolved with chloroform and went quickly through a short silica gel column with chloroform as eluent. The majority of chloroform in the derived solution was removed via vacuum and the residue was precipitated into 100 mL methanol again. Following, the precipitate was filtered and subjected to Soxhlet extraction with methanol, hexane, and chloroform for 8.0 h, successively. After that, the majority of chloroform in the mixture was removed by vacuum and the residue was precipitated into 100 mL methanol again. Finally, the mixture was centrifuged to obtain the crude product and dried under vacuum overnight to get the target product (73.8 mg, 76.4%). SEC (THF):  $M_n = 10.5 \text{ kg mol}^{-1}$ ;  $M_w = 18.4 \text{ kg mol}^{-1}$ ;  $\bar{D} = 1.75$ .  $^1\text{H-NMR}$  (400 MHz,  $\text{CDCl}_3$ ,  $\delta$  ppm): 7.13–6.67 (br, 5H), 3.09–2.93 (br, 3H), 0.96–0.90 (br, 14H). FTIR ( $\text{cm}^{-1}$ ): 3081, 2926, 2852, 1628, 1437, 998, 793. Anal. Calcd for  $(\text{C}_{21}\text{H}_{22}\text{O}_3\text{S}_2)_n$ : C, 65.25; H, 5.74; O, 12.42; S, 16.59. Found: C, 65.01; H, 5.49.

**Synthesis of PF2:** PF2 was synthesized following the similar procedures as PF1. Finally, PF2 (107.1 mg) was obtained with yield of 85.9%. GPC (THF):  $M_n = 30.1 \text{ kg mol}^{-1}$ ;  $M_w = 49.7 \text{ kg mol}^{-1}$ ;  $\bar{D} = 1.65$ .  $^1\text{H-NMR}$  (400 MHz,  $\text{CDCl}_3$ ,  $\delta$  ppm): 7.15–6.79 (br, 5H), 3.00–2.92 (br, 3H), 0.98–0.88 (br, 30H). FTIR ( $\text{cm}^{-1}$ ): 3069, 2933, 2853, 1635, 1437, 997, 793. Anal. Calcd for  $(\text{C}_{29}\text{H}_{38}\text{O}_3\text{S}_2)_n$ : C, 69.84; H, 7.68; O, 9.62; S, 12.86. Found: C, 69.35; H, 9.31.

**Device Fabrication and Characterization:** OSCs were fabricated with an inverted structure of ITO/M-ZnO (35 nm)/PTs:m-ITIC/MoO<sub>x</sub> (9 nm)/Ag (100 nm). First, the patterned ITO-coated glass ( $15 \Omega \text{ sq}^{-1}$ ) was successively cleaned by ultrasonic treatment in detergent, deionized water, acetone, and isopropanol for 30 min. Then, the ITO-coated glass was dried with nitrogen-flow, and irradiated with oxygen plasma for 20 min. Next, the ZnO precursor solution prepared according to the reported literature was spin-coated on top of the ITO-coated glass with spin-coating rate of 4500 rpm for 30 s.<sup>[64]</sup> And the above film was annealed at 220 °C for 40 min in air. Following, 0.9 wt% trisiloxane small molecule in isopropanol was spin-coated on ZnO film, which was then thermally annealed at 120 °C for 8 min in air to obtain the M–ZnO film. The PTs:m-ITIC or PF2:m-ITIC:PC<sub>71</sub>BM blends were dissolved in chlorobenzene and stirred at 70 °C for at least 2.0 h in glovebox ( $V_{\text{O}_2} < 0.1 \text{ ppm}$ ,  $V_{\text{H}_2\text{O}} < 0.1 \text{ ppm}$ ). Before spin-coating, some diphenyl ether (DPE) were added into the chlorobenzene solution and stirred at 70 °C for at least 1.0 h. The active layer solution was spin-coated onto the M–ZnO film, and then annealed at 130 or 150 °C for 5 min. Finally, MoO<sub>x</sub> (9 nm) and Ag (100 nm) were successively evaporated onto the active layer under pressure of  $4.0 \times 10^{-4} \text{ Pa}$ . The active area of the devices was 4.0 mm<sup>2</sup> determined by the mask. The current density-voltage (*J*–*V*) characteristics of OSCs were measured via Keithley 2400 source-meter under AM 1.5G simulated by a Newport-Oriel solar simulator, where the light intensity was calibrated to 1000 W m<sup>-2</sup> using an NREL-certified single crystal silicon cell. EQE spectra were measured with a commercial photo modulation spectroscopy setup that included a Xenon lamp, an optical chopper, a monochromator, and a lock-in amplifier operated by a PC computer. Meanwhile, a calibrated Si photodiode was used as a standard in the EQE measurement. The PCE statistics were obtained using 20 individual devices fabricated under the same optimized condition.

## Supporting Information

Supporting Information is available from the Wiley Online Library or from the author.

## Acknowledgements

This work is financially supported by the National Key Research and Development Program of China (No. 2017YFA0206600), the Program of the Chinese Academy of Sciences (Grant No. XDB43000000), the Postdoctoral Fund of China (No. FJ3050A0670111), the Science and

Technology Development Project of Henan Province (No. 202300410057, 202300410048), the Intelligence Introduction Plan of Henan Province in 2021 (CXJD2021008), the Henan University Fund, the German Research Foundation (DFG: LE 2249/5-1) and the Sino-German Center for Research Promotion (GZ1579).

Open access funding enabled and organized by Projekt DEAL.

## Conflict of Interest

The authors declare no conflict of interest.

## Data Availability Statement

The data that supports the findings of this study are available in the supplementary material of this article.

## Keywords

electron donors, furan-3-carboxylate, non-fused-ring polymers, organic solar cells, synthetic complexity

Received: August 3, 2021

Revised: October 8, 2021

Published online: November 27, 2021

- [1] A. J. Heeger, *Adv. Mater.* **2014**, *26*, 10.
- [2] G. Li, W.-H. Chang, Y. Yang, *Nat. Rev. Mater.* **2017**, *2*, 17043.
- [3] S. Pang, R. Zhang, C. Duan, S. Zhang, X. Gu, X. Liu, F. Huang, Y. Cao, *Adv. Energy Mater.* **2019**, *9*, 1901740.
- [4] Z. Wang, K. Gao, Y. Kan, M. Zhang, C. Qiu, L. Zhu, Z. Zhao, X. Peng, W. Feng, Z. Qian, X. Gu, A. K. Y. Jen, B. Z. Tang, Y. Cao, Y. Zhang, F. Liu, *Nat. Commun.* **2021**, *12*, 332.
- [5] Y. Lin, M. I. Nugraha, Y. Firdaus, A. D. Scaccabarozzi, F. Aniés, A.-H. Emwas, E. Yengel, X. Zheng, J. Liu, W. Wahyudi, E. Yarali, H. Faber, O. M. Bakr, L. Tsetseris, M. Heeney, T. D. Anthopoulos, *ACS Energy Lett.* **2020**, *5*, 3663.
- [6] Q. Liu, Y. Jiang, K. Jin, J. Qin, J. Xu, W. Li, J. Xiong, J. Liu, Z. Xiao, K. Sun, S. Yang, X. Zhang, L. Ding, *Sci. Bull.* **2020**, *65*, 272.
- [7] G. Liu, R. Xia, Q. Huang, K. Zhang, Z. Hu, T. Jia, X. Liu, H. L. Yip, F. Huang, *Adv. Funct. Mater.* **2021**, *31*, 2103283.
- [8] R. Shen, Z. Sun, Y. Shi, Y. Zhou, W. Guo, Y. Zhou, H. Yan, F. Liu, *ACS Nano* **2021**, *15*, 6296.
- [9] L. Zhan, S. Li, X. Xia, Y. Li, X. Lu, L. Zuo, M. Shi, H. Chen, *Adv. Mater.* **2021**, *33*, 2007231.
- [10] M. Zhang, L. Zhu, G. Zhou, T. Hao, C. Qiu, Z. Zhao, Q. Hu, B. W. Larson, H. Zhu, Z. Ma, Z. Tang, W. Feng, Y. Zhang, T. P. Russell, F. Liu, *Nat. Commun.* **2021**, *12*, 309.
- [11] R. Po, G. Bianchi, C. Carbonera, A. Pellegrino, *Macromolecules* **2015**, *48*, 453.
- [12] C. Sun, F. Pan, H. Bin, J. Zhang, L. Xue, B. Qiu, Z. Wei, Z. G. Zhang, Y. Li, *Nat. Commun.* **2018**, *9*, 743.
- [13] X. Li, F. Pan, C. Sun, M. Zhang, Z. Wang, J. Du, J. Wang, M. Xiao, L. Xue, Z. G. Zhang, C. Zhang, F. Liu, Y. Li, *Nat. Commun.* **2019**, *10*, 519.
- [14] D. Yuan, F. Pan, L. Zhang, H. Jiang, M. Chen, W. Tang, G. Qin, Y. Cao, J. Chen, *Sol. RRL* **2020**, *4*, 2000062.
- [15] S. Bekir, M. Talu, F. Yildirim, E. K. Balci, *Appl. Surf. Sci.* **2003**, *205*, 23.
- [16] J. W. Jo, J. W. Jung, H.-W. Wang, P. Kim, T. P. Russell, W. H. Jo, *Chem. Mater.* **2014**, *26*, 4214.
- [17] F. González, P. Tiemblo, M. Hoyos, *Appl. Sci.* **2019**, *9*, 3371.

- [18] X. Jia, Z. Chen, C. Duan, Z. Wang, Q. Yin, F. Huang, Y. Cao, *J. Mater. Chem. C* **2019**, *7*, 314.
- [19] X. Jia, G. Liu, S. Chen, Z. Li, Z. Wang, Q. Yin, H.-L. Yip, C. Yang, C. Duan, F. Huang, Y. Cao, *ACS Appl. Energy Mater.* **2019**, *2*, 7572.
- [20] Q. Wang, Y. Qin, M. Li, L. Ye, Y. Geng, *Adv. Energy Mater.* **2020**, *10*, 2002572.
- [21] Z. Liang, M. Li, Q. Wang, Y. Qin, S. J. Stuard, Z. Peng, Y. Deng, H. Ade, L. Ye, Y. Geng, *Joule* **2020**, *4*, 1278.
- [22] J. Ren, P. Bi, J. Zhang, J. Liu, J. Wang, Y. Xu, Z. Wei, S. Zhang, J. Hou, *Natl. Sci. Rev.* **2021**.
- [23] Q. Wang, M. Li, Z. Peng, N. Kirby, Y. Deng, L. Ye, Y. Geng, *Sci. China: Chem.* **2021**, *64*, 478.
- [24] J. Xiao, X. Jia, C. Duan, F. Huang, H. L. Yip, Y. Cao, *Adv. Mater.* **2021**, *33*, 2008158.
- [25] G. Wang, P. Kumar, Z. Zhang, A. D. Hendsbee, H. Liu, X. Li, J. Wang, Y. Li, *RSC Adv.* **2020**, *10*, 12876.
- [26] O. Gidron, A. Dadvand, Y. Sheynin, M. Bendikov, D. F. Perepichka, *Chem. Commun.* **2011**, *47*, 1976.
- [27] P. Huang, J. Du, M. C. Biewer, M. C. Stefan, *J. Mater. Chem. A* **2015**, *3*, 6244.
- [28] B. Li, *Chin. J. Org. Chem.* **2015**, *35*, 2487.
- [29] J. Warnan, C. Cabanetos, A. El Labban, M. R. Hansen, C. Tassone, M. F. Toney, P. M. Beaujuge, *Adv. Mater.* **2014**, *26*, 4357.
- [30] L. Huo, T. Liu, B. Fan, Z. Zhao, X. Sun, D. Wei, M. Yu, Y. Liu, Y. Sun, *Adv. Mater.* **2015**, *27*, 6969.
- [31] A. Gandini, M. N. Belgacem, *Prog. Polym. Sci.* **1997**, *22*, 1203.
- [32] J. B. Binder, R. T. Raines, *J. Am. Chem. Soc.* **2009**, *131*, 1979.
- [33] X. Hu, S. Jiang, S. Kadarwati, D. Dong, C.-Z. Li, *RSC Adv.* **2016**, *6*, 40489.
- [34] M. Zhang, X. Guo, Y. Yang, J. Zhang, Z.-G. Zhang, Y. Li, *Polym. Chem.* **2011**, *2*, 2900.
- [35] W. R. Mateker, J. D. Douglas, C. Cabanetos, I. T. Sachs-Quintana, J. A. Bartelt, E. T. Hoke, A. El Labban, P. M. Beaujuge, J. M. J. Fréchet, M. D. McGehee, *Energy Environ. Sci.* **2013**, *6*, 2529.
- [36] S. Chen, Y. An, G. K. Dutta, Y. Kim, Z.-G. Zhang, Y. Li, C. Yang, *Adv. Funct. Mater.* **2017**, *27*, 1603564.
- [37] Y. Jin, Z. Chen, M. Xiao, J. Peng, B. Fan, L. Ying, G. Zhang, X.-F. Jiang, Q. Yin, Z. Liang, F. Huang, Y. Cao, *Adv. Energy Mater.* **2017**, *7*, 1700944.
- [38] Z. Zhao, H. Nie, C. Ge, Y. Cai, Y. Xiong, J. Qi, W. Wu, R. T. K. Kwok, X. Gao, A. Qin, J. W. Y. Lam, B. Tang, *Adv. Sci.* **2017**, *4*, 1700005.
- [39] Y. Gao, Z. Wang, G. Yue, X. Yu, X. Liu, G. Yang, F. Tan, Z. Wei, W. Zhang, *Sol. RRL* **2019**, *3*, 1900012.
- [40] Y. Gao, Z. Shen, F. Tan, G. Yue, R. Liu, Z. Wang, S. Qu, Z. Wang, W. Zhang, *Nano Energy* **2020**, *76*, 104964.
- [41] Y. Gao, X. Gao, Z. Su, S. Qu, W. Zhang, S. He, Z. Wang, S. Lu, G. Dong, G. Yue, F. Tan, Z. Wang, *J. Mater. Chem. C* **2021**, *9*, 13500.
- [42] K. Maex, M. R. Baklanov, D. Shamiryman, F. Iacopi, S. H. Brongersma, Z. S. Yanovitskaya, *J. Appl. Phys.* **2003**, *93*, 8793.
- [43] J. Du, A. Fortney, K. E. Washington, M. C. Biewer, T. Kowalewski, M. C. Stefan, *J. Mater. Chem. A* **2017**, *5*, 15591.
- [44] Q. Fan, W. Su, X. Guo, X. Zhang, Z. Xu, B. Guo, L. Jiang, M. Zhang, Y. Li, *J. Mater. Chem. A* **2017**, *5*, 5106.
- [45] M. C. Scharber, D. Mühlbacher, M. Koppe, P. Denk, C. Waldauf, A. J. Heeger, C. J. Brabec, *Adv. Mater.* **2006**, *18*, 789.
- [46] Y. Qin, M. A. Uddin, Y. Chen, B. Jang, K. Zhao, Z. Zheng, R. Yu, T. J. Shin, H. Y. Woo, J. Hou, *Adv. Mater.* **2016**, *28*, 9416.
- [47] H. Yao, D. Qian, H. Zhang, Y. Qin, B. Xu, Y. Cui, R. Yu, F. Gao, J. Hou, *Chin. J. Chem.* **2018**, *36*, 491.
- [48] Q. Wang, M. Li, X. Zhang, Y. Qin, J. Wang, J. Zhang, J. Hou, R. A. J. Janssen, Y. Geng, *Macromolecules* **2019**, *52*, 4464.
- [49] Y. Yang, Z. G. Zhang, H. Bin, S. Chen, L. Gao, L. Xue, C. Yang, Y. Li, *J. Am. Chem. Soc.* **2016**, *138*, 15011.
- [50] P. Bi, T. Xiao, X. Yang, M. Niu, Z. Wen, K. Zhang, W. Qin, S. K. So, G. Lu, X. Hao, H. Liu, *Nano Energy* **2018**, *46*, 81.
- [51] W. Yang, W. Wang, Y. Wang, R. Sun, J. Guo, H. Li, M. Shi, J. Guo, Y. Wu, T. Wang, G. Lu, C. J. Brabec, Y. Li, J. Min, *Joule* **2021**, *5*, 1209.
- [52] H. Bin, L. Gao, Z. G. Zhang, Y. Yang, Y. Zhang, C. Zhang, S. Chen, L. Xue, C. Yang, M. Xiao, Y. Li, *Nat. Commun.* **2016**, *7*, 13651.
- [53] Y. Li, X. Liu, F. Wu, Y. Zhou, Z. Jiang, B. Song, Y. Xia, Z. Zhang, F. Gao, O. Inganäs, Y. Li, L. Liao, *J. Mater. Chem. A* **2016**, *4*, 5890.
- [54] G. Chen, C. Han, L. Yan, Y. Li, Y. Zhao, X. Zhang, *J. Semicond.* **2019**, *40*, 122701.
- [55] P. Wang, G. Li, M. Wang, H. Li, J. Zheng, L. Yang, Y. Chen, D. Li, L. Lu, *J. Semicond.* **2020**, *41*, 062701.
- [56] B. Fan, K. Zhang, X. F. Jiang, L. Ying, F. Huang, Y. Cao, *Adv. Mater.* **2017**, *29*, 1606396.
- [57] Y. You, W. Tian, M. Wang, F. Cao, H. Sun, L. Li, *Adv. Mater. Interfaces* **2020**, *7*, 2000537.
- [58] L. Ye, Y. Jing, X. Guo, H. Sun, S. Zhang, M. Zhang, L. Huo, J. Hou, *J. Phys. Chem. C* **2013**, *117*, 14920.
- [59] P. Guo, G. Luo, Q. Su, J. Li, P. Zhang, J. Tong, C. Yang, Y. Xia, H. Wu, *ACS Appl. Mater. Interfaces* **2017**, *9*, 10937.
- [60] M. Chen, B. Zhao, J. Xin, Z. Cong, X. Li, L. Yang, W. Ma, W. Wei, C. Gao, *Dyes Pigm.* **2019**, *161*, 58.
- [61] Y. Cui, S. Zhang, N. Liang, J. Kong, C. Yang, H. Yao, L. Ma, J. Hou, *Adv. Mater.* **2018**, *30*, 1802499.
- [62] R. Sun, Q. Wu, J. Guo, T. Wang, Y. Wu, B. Qiu, Z. Luo, W. Yang, Z. Hu, J. Guo, M. Shi, C. Yang, F. Huang, Y. Li, J. Min, *Joule* **2020**, *4*, 407.
- [63] Y. Zhang, D. Deng, Q. Wu, Y. Mi, C. Yang, X. Zhang, Y. Yang, W. Zou, J. Zhang, L. Zhu, H. Zhou, X. Liu, Z. Wei, *Sol. RRL* **2020**, *4*, 1900580.
- [64] Y. Sun, J. H. Seo, C. J. Takacs, J. Seifert, A. J. Heeger, *Adv. Mater.* **2011**, *23*, 1679.